



Simulation of Rock Crack Propagation and Failure Behavior Based on a Mixed Failure Model with SPH

Man Hu¹ · Qiuting Tan¹ · Dianlei Feng² · Yi Ren¹ · Yu Huang³

Received: 11 September 2023 / Accepted: 30 May 2024

© The Author(s), under exclusive licence to Springer-Verlag GmbH Austria, part of Springer Nature 2024

Abstract

Understanding the mechanisms of crack propagation and failure behavior in rocks is fundamental for geotechnical engineering and mining applications. This study employs a coupled damage model based on the Smoothed Particle Hydrodynamics (SPH) method that integrates the Drucker–Prager and Grady–Kipp models. This mixed failure model is then implemented to simulate the crack propagation morphology and failure modes in uniaxial compression tests of flawed rock samples, and validated against multiple experimental observations. The numerical results exhibit good agreement with experimental observations from the literature in terms of the initiation and propagation of tensile and shear fractures, as well as the final failure morphology. Additionally, this work incorporates contact algorithms to simulate the loading plates, thereby better representing the actual experimental conditions encountered in uniaxial compression tests. Furthermore, a comprehensive parametric study is conducted to investigate the influence of key factors, such as pre-flaw geometry, cohesion, friction at the loading plate interface, and discretization parameters, on the simulated fracture processes and mechanical response. The outcomes indicate the proposed coupled damage model within the SPH framework can accurately capture complex fracture patterns and failure mechanisms in uniaxial compression of flawed rocks. This work demonstrates the capability of the SPH-based mixed-mode failure model to provide insights into rock fracture and failure mechanisms.

Highlights

- A coupled damage model integrating the Drucker–Prager and Grady–Kipp criteria within a smoothed particle hydrodynamics (SPH) framework is applied to simulate both shear and tensile failure modes in rocks firstly. The model is validated against more experimental observations, demonstrating the model's ability to reproduce the crack propagation and characteristic stress–strain behavior.
- This work presents a comprehensive parametric study investigating the influence of key factors, such as pre-flaw geometry, cohesion, friction at the loading plate interface, and discretization parameters, on the simulated fracture processes and mechanical response. These systematic investigations provide valuable insights into the governing mechanisms and highlight the importance of proper model calibration for accurate predictions.
- This work incorporates contact algorithms to simulate the loading plates, thereby better representing the actual experimental conditions encountered in uniaxial compression tests. The tensile wing cracks subjected to uniaxial compression, oriented vertically towards the top boundary of the specimen, are successfully captured.

Keywords Mixed-mode failure model · Smoothed particle hydrodynamics (SPH) · Crack propagation · Rock failure · Uniaxial compression

✉ Man Hu
humanyyes@swu.edu.cn

✉ Yu Huang
yhuang@tongji.edu.cn

¹ College of Engineering and Technology, Southwest University, Chongqing 400715, China

² Department of Hydraulic Engineering College of Civil Engineering, Tongji University, Shanghai 200092, China

³ Department of Geotechnical Engineering College of Civil Engineering, Tongji University, Shanghai 200092, China

1 Introduction

Rock fragmentation, crack propagation, and post-failure behavior are pivotal topics in rock mechanics and engineering. Domains spanning mining, tunneling, geological disposal of radioactive waste, hydrocarbon extraction, geothermal energy exploitation, and reservoir geomechanics all critically rely on accurate predictions of crack growth and failure evolution in rock materials. Over the years, researchers have made significant progress in understanding the process of crack initiation, propagation, and coalescence in rock through both empirical studies and theoretical analyses (Zhai et al. 2016; Deng et al. 2020; Zheng et al. 2021; Liu et al. 2023). Simulating these phenomena accurately can provide researchers and professionals with a more comprehensive understanding of the mechanical properties of rock materials.

Historically, numerical approaches grounded in classical fracture mechanics principles, notably the finite element method (FEM), have been extensively employed as the predominant techniques for simulating crack propagation in rocks. As a widely-used approach, FEM can explore fracture propagation and merging in both two- and three-dimensional settings (Yang et al. 2015; Cheng et al. 2023). Nevertheless, FEM often encounter formidable challenges when attempting to handle discontinuities, large deformations, and the emergence of intricate, tortuous fracture patterns that are characteristic of rock failure processes under complex stress states.

In recent years, emerging techniques like phase-field methods, extended finite element methods (XFEM), discrete element methods (DEM), and molecular dynamics simulations under periodic boundary conditions have provided new avenues and tools for more precisely modeling rock material failure processes. The phase-field method relates crack extension to the evolution of a phase-field variable and simulates crack initiation and propagation by solving the governing phase-field equations, offering unique advantages in handling cracks with arbitrary geometries. The phase field damage model has been effectively employed to simulate tensile and compressive crack initiation and propagation in brittle fracture with high accuracy (Ambati et al. 2015; Bleyer and Alessi 2018), but it requires a large computational cost as it necessitates discretization of the entire computational domain and solution of the phase field and other auxiliary field variables. Additionally, the model involves several sensitive parameters, whose selection affects the accuracy and convergence of the simulation results. The XFEM emerged as an enhancement over traditional FEM, introducing additional degrees of freedom localized around discontinuities to better capture the kinematics of crack propagation (Eftekhari et al. 2016; Zhou

and Chen 2019). Nevertheless, XFEM still requires a priori knowledge of potential crack paths and enrichment functions, thereby limiting its generality and applicability to scenarios where such information is unavailable or difficult to ascertain. DEM has gained popularity in the study of rock fractures due to its ability to model the complex mechanical behavior of rocks at the particle scale, allowing for the evaluation of fracture initiation, propagation, and evolution (Jiang et al. 2015). While powerful, DEM has limitations in computational expenses, uncertainties in material properties and boundary conditions, and may not fully capture all fracture mechanisms. Thus, it is often coupled with other methods (Sun et al. 2013). Molecular dynamics simulations under periodic boundary conditions have also gained attention as an advanced approach for fracture modeling in recent years, however it is limited by high computational cost, which restricts the accessible time and length scales, and the potential inaccuracies arising from empirical interatomic potentials and periodic boundary conditions that may not capture realistic crack behavior. As an alternative, NMM represents materials using interacting surfaces or manifolds instead of traditional element grids or meshes, gaining popularity for modeling complex fracture geometries and propagation (Fan et al. 2021b). However, NMM has challenges in computational cost for large-scale problems as it requires a large number of manifolds to be constructed and updated. Additionally, the accuracy of NMM can be affected by the choice of partitioning schemes, regularizations, and other factors (Fan et al. 2021a). Recently, the non-local, mesh-free PD method has shown promise by modeling materials as interacting particles (Niu et al. 2023). Yet there are also some limitations in computational cost from its non-local formulation and accuracy dependent on parameter selection (Giannakeas et al. 2020).

Substantial efforts have been dedicated to improving the accuracy of crack propagation and failure modeling in rocks. Classical approaches based on fracture mechanics principles, such as energy-based approach (Bekele et al. 2020), stress intensity factors (Demchina et al. 2022), and J-integral analyses (Carrier and Granet 2012), have been widely employed. According to the classical theory of brittle fracture, if the strain energy surrounding the crack tip surpasses the energy requisite for generating new surfaces, then the crack will begin to spread (Lajtai 1971; Li et al. 2007). The energy-based approach is a promising and widely used method for predicting crack propagation. For instance, it may not fully capture material behaviors during the pre-fracture and post-fracture stages, as it does not account for the complex strain/stress state surrounding the crack tip. The recognition that a crack can attenuate the material around it has led to the incorporation of an additional variable in the strain–stress relationship. Recently researchers have also explored integrating damage mechanisms and constitutive models to

simulate crack propagation. Kachanov's damage theory has been successfully applied in FEM analyses and extended to model crack evolution in anisotropic materials. Additionally, comprehensive failure models, such as the Deshpande–Evans model, Rajendran–Grove(RG) model, Continuous damage constitutive model, Johnson–Holmquist (JH) model, JH II, Holmquist–Johnson–Cook(HJC) model and Riedel–Hiermaier–Thoma(RHT) have emerged in related fields, offering new perspectives on simulating crack propagation and ultimate failure by incorporating various failure mechanisms. For example, Keller and Hutter (2014) established a viscoelastic damage model based on the Weibull function, but it did not consider the healing effect under high compressive stresses. Liu et al. (2016) proposed a novel damage model founded on energy dissipation to describe the behavior of rocks under cyclic loading, but focused only on model development and validation under cyclic loading. Fu et al. (2017) proposed an elastic-brittle model to simulate the failure mechanism of brittle rocks. Despite these advancements, accurately simulating crack behavior in rocks remains a formidable challenge due to the heterogeneity, anisotropy, and complexity of fracture propagation processes in these materials, necessitating further development of advanced numerical methods and constitutive models.

Apart these methods, SPH has attracted increasing attention in recent years due to its advantages in simulating large deformation and discontinuous material behaviors. As a truly meshfree, fully Lagrangian approach, SPH discretizes the computational domain into particles that interact with each other via kernel approximations, circumventing the need for a fixed mesh or remeshing procedures (Bui et al. 2008). This inherent meshfree nature endows SPH with a unique advantage in naturally handling discontinuities and large deformations. The approach has been utilized with great success on a wide range of problems, covering elastic flow, fluid flow, impact issues, thermal conduction, multiphase flow, geophysical flow, fluid–structure interaction, the post-failure of both cohesive and non-cohesive soils, and fracture of rock (Bui, et al. 2007; Bui and Fukagawa 2013; Huang et al. 2015; Douillet-Grellier et al. 2016; Mu et al. 2022).

Despite these merits, the accuracy and reliability of fracture modeling in SPH critically hinge on the constitutive formulations employed to represent the underlying mechanisms governing material failure. For shear failure, one of the most important constitutive models for SPH simulations of capturing plasticity and shear failure is the Drucker–Prager (DP) model, which defines the plasticity and failure criteria of materials based on the yield surface and the flow rule (Drucker and Prager 1952; Drucker et al. 1952). The Drucker–Prager model has been widely used in SPH simulations to capture plasticity and shear failure in various materials, including large deformation in granular materials, the shear box tests, and failures in

jointed media (Kaus 2010; Singh et al. 2019; Zhang and Zhou 2023). However, a limitation of the DP model is that it does not account for the effects of tensile stress, which is common in rock cracking and fragmentation. On the other hand, the Grady–Kipp damage model, based on the energy conservation criteria and statistical fracture analysis, has proven effective for simulating tensile failure in brittle materials under high-speed impacts, failure in magma chambers, and the penny-shaped crack problem. To develop a more holistic approach, Douillet-Grellier et al. (2016) proposes a coupled model that synergistically combines the Drucker–Prager plasticity formulation and the Grady–Kipp tensile damage criteria within an SPH framework in order to simulate mode I, mode II and mixed mode failure under the same formulation. The model is applied to study failure in uniaxial compression of gypsum samples containing a single angled flaw, demonstrating good ability to simulate crack propagation, and has also been well described in studying the propagation process under different prefabricated crack angles.

The present work builds upon the pioneering coupled model developed by Douillet-Grellier et al. (2016), which synergistically combined the Drucker–Prager plasticity formulation and the Grady–Kipp tensile damage criteria within a smoothed particle hydrodynamics (SPH) framework. Inspired by their approach, extensive research efforts are undertaken to further advance the modeling capabilities and address certain limitations. Firstly, the scope of the investigation is expanded by conducting a comprehensive parametric study investigating the influence of key factors, such as pre-flaw geometry, cohesion, friction at the loading plate interface, and discretization parameters on the simulated fracture patterns. Secondly, while previous studies simplified the loading plates as non-slip boundary conditions, our implementation incorporates contact algorithms to simulate the pressurized loading plates, thereby better representing the actual experimental conditions encountered in uniaxial compression tests, providing valuable insights into boundary effects on crack initiation and propagation. Thirdly, a comprehensive study is performed by comparing the simulation results against the experimental data from literature.

2 The SPH Method

The basic idea of the SPH method is to discretize into a group of points with material properties, and interact with all neighboring particles through a smooth kernel function.

2.1 The Basic of SPH Method

The core of the Smoothed Particle Hydrodynamics (SPH) is to construct kernel function:

$$\langle f(x) \rangle = \int_{\Omega} f(x') W(x - x', h) dx' \tag{1}$$

where W is the kernel function, h is the smoothing length, which defines the influence domain of W . This article adopts the most widely used cubic spline function proposed by Monaghan and Lattanzio, which has the following form:

$$W_{ij} = \alpha_d \times \begin{cases} \frac{2}{3} - q^2 + \frac{1}{2}q^3, & 0 \leq q \leq 1 \\ \frac{1}{6}(2 - q)^3, & 1 \leq q < 2 \\ 0, & q \geq 2 \end{cases} \tag{2}$$

where α_d is $\frac{1}{h^3} \frac{15}{7\pi h^2}$, $\frac{3}{2\pi h^3}$ in one-, two- and three-dimensional space, respectively. q is the relative distance between particle x and x' , and $q = \frac{r}{h} = \frac{|x-x'|}{h}$.

Equation (1) can be discretized into the following form:

$$\langle f(x) \rangle \approx \sum_{j=1}^N \frac{m_j}{\rho_j} f(x_j) W(x - x_j, h) \tag{3}$$

where m_j and ρ_j are, respectively, the mass and the density of particle j .

2.2 Governing Equations

The governing equations under the SPH framework consist of a mass control equation and a momentum control equation (Tran et al. 2019):

$$\frac{D\rho}{Dt} = -\rho \nabla \cdot \mathbf{v} \tag{4}$$

$$\frac{D\mathbf{v}}{Dt} = \frac{1}{\rho} \nabla \cdot \boldsymbol{\sigma} + \mathbf{g} \tag{5}$$

where ρ is the density; \mathbf{v} is the velocity; $\boldsymbol{\sigma}$ is the stress tensor; \mathbf{g} is the external force.

2.3 Constitutive Equation of Rock

In this study, the elastic–plastic constitutive (Bui et al. 2008) model will be used to describe the rock behavior. In the elastic–plastic constitutive model, $\dot{\epsilon}^{\alpha\beta}$ is normally composed of elastic strain rate tensor $\dot{\epsilon}_e^{\alpha\beta}$ and plastic strain rate tensor $\dot{\epsilon}_p^{\alpha\beta}$:

$$\dot{\epsilon}^{\alpha\beta} = \dot{\epsilon}_e^{\alpha\beta} + \dot{\epsilon}_p^{\alpha\beta} \tag{6}$$

It can be expressed in the following form for $\dot{\epsilon}_e^{\alpha\beta}$ and $\dot{\epsilon}_p^{\alpha\beta}$:

$$\dot{\epsilon}_e^{\alpha\beta} = \frac{\dot{s}^{\alpha\beta}}{2G} + \frac{1 - 2\nu}{3E} \dot{\sigma}^{\gamma\gamma} \delta^{\alpha\beta} \tag{7}$$

$$\dot{\epsilon}_p^{\alpha\beta} = \lambda \frac{\partial g}{\partial \sigma^{\alpha\beta}} \tag{8}$$

The plasticity operator can be calculated as follows

$$\lambda = \frac{3\alpha K \dot{\epsilon}^{\gamma\gamma} + \left(G/\sqrt{J_2}\right) s^{\alpha\beta} \dot{\epsilon}^{\alpha\beta}}{27\alpha_\phi K \sin\Psi + G} \tag{9}$$

Herein $\dot{\epsilon}^{\alpha\beta}$ can be expressed as adding the two

$$\dot{\epsilon}^{\alpha\beta} = \frac{\dot{s}^{\alpha\beta}}{2G} + \frac{1 - 2\nu}{3E} \dot{\sigma}^{\gamma\gamma} \delta^{\alpha\beta} + \lambda \frac{\partial g}{\partial \sigma^{\alpha\beta}} \tag{10}$$

$$\dot{\epsilon}_{\alpha\beta} = \frac{1}{2} \left(\frac{\partial v^\alpha}{\partial x^\beta} + \frac{\partial v^\beta}{\partial x^\alpha} \right) \tag{11}$$

According to Eq. (5), the SPH form of the Navier Stocks equation can be obtained

$$\frac{Dv_i^\alpha}{Dt} = \sum_{j=1}^N m_j \left(\frac{\sigma_i^{\alpha\beta}}{\rho_i^2} + \frac{\sigma_j^{\alpha\beta}}{\rho_j^2} \right) \cdot \frac{\partial W_{ij}}{\partial x_i^\beta} + f^\alpha \tag{12}$$

3 Key Numerical Techniques

Simulations using SPH without any tensile instability treatment may result in numerical instability. This article discusses three numerical methods to mitigate tensile instability in SPH simulations.

3.1 Artificial Viscosity

To avoid nonphysical oscillations caused by SPH solution results, this paper uses the widely used Monaghan type artificial viscosity (Monaghan 1992), so Eq. (12) can be expressed as

$$\frac{Dv_i^\alpha}{Dt} = \sum_{j=1}^N m_j \left(\frac{\sigma_i^{\alpha\beta}}{\rho_i^2} + \frac{\sigma_j^{\alpha\beta}}{\rho_j^2} - \Pi_{ij} \delta^{\alpha\beta} \right) \cdot \frac{\partial W_{ij}}{\partial x_i^\beta} + f^\alpha \tag{13}$$

where Π_{ij} is the artificial viscosity, which is applied to resolve the unphysical oscillation, and is given by:

$$\prod_{ij} = \begin{cases} \frac{-\alpha_n \bar{c}_{ij} \phi_{ij} + \beta_n \phi_{ij}^2}{\rho_{ij}}, & \mathbf{v}_{ij} \cdot \mathbf{x}_{ij} < 0 \\ 0, & \mathbf{v}_{ij} \cdot \mathbf{x}_{ij} \geq 0 \end{cases} \quad (14)$$

3.2 Artificial Stress

This article introduces the artificial stress technique (Monaghan 2000; Gray et al. 2001), which alleviates tensile instability by introducing a short-range repulsive force between adjacent particle pairs. This repulsive force prevents excessive particle clustering and thereby mitigates tensile instability.

$$\frac{Dv_i^\alpha}{Dt} = \sum_{j=1}^N m_j \left(\frac{\sigma_i^{\alpha\beta}}{\rho_i^2} + \frac{\sigma_j^{\alpha\beta}}{\rho_j^2} - \Pi_{ij} \delta^{\alpha\beta} + f_{ij}^n (R_{\epsilon_i} + R_{\epsilon_j}) \right) \cdot \frac{\partial W_{ij}}{\partial x_i^\beta} + f^\alpha \quad (15)$$

where n is the exponent dependent on the smoothing kernel; f_{ij} is the repulsive force term, it can be represented as according to Monaghan:

$$f_{ij} = \frac{W_{ij}}{W(\Delta d, h)} \quad (16)$$

where Δd is the particle spacing, h is assumed to be constant.

3.3 XSPH Correction

The XSPH correction (Douillet-Grellier et al. 2016) can be used to reduce tensile instability by assigning each particle an averaged velocity from its neighboring particles. The XSPH velocity correction for particle i is expressed as:

$$\frac{Dx_i}{Dt} = v_i + \bar{\epsilon} \sum_{j \in \Lambda_i} \frac{m_j}{\rho_{ij}} v_{ij} W_{ij} \quad (17)$$

The parameter $\bar{\epsilon}$ lies between 0.0 and 1.0. In this work, $\bar{\epsilon} = 0.5$.

4 Establishment of Mixed-Mode Failure Model

4.1 Shear Failure Model

The pioneering work of Bui et al. incorporated the Drucker–Prager plasticity model in a SPH framework, enabling researchers to analyze a variety of failure conditions such as soil collapse, slope stability, compression failure, jointed media failure, large deformation, and shear

box laboratory experiments within a multiscale modeling approach (Bui et al. 2007, 2008; Bui and Fukagawa 2013). Through a modification of the Mohr–Coulomb criterion, the Drucker–Prager yield criterion is expressed as:

$$F(I_1, J_2) = \sqrt{J_2} + \alpha_\phi I_1 - k_c \quad (18)$$

where c is the cohesion of the rock, J_2 is the second principal invariant of the deviatoric stress tensor, and I_1 is the first invariant of the stress tensor. The parameters α_ϕ and k_c are given by

$$\alpha_\phi = \frac{\tan \phi}{\sqrt{9 + 12 \tan^2 \phi}} k_c = \frac{3c}{\sqrt{9 + 12 \tan^2 \phi}} \quad (19)$$

where ϕ is the internal friction angle of the rock.

It is noteworthy that the Drucker–Prager model, incorporating a non-associative flow rule, is regularly employed to evaluate the failure process of rock.

To account for rock strength degradation under loading conditions, a cohesive softening constitutive relationship was incorporated to the Drucker–Prager model. In this study, the cohesive force c is linearly related to the cumulative plastic strain $\bar{\epsilon}_p$, and the cohesive force softens accordingly based on the value of the $\bar{\epsilon}_p$. The functional relationship between cohesion and cumulative plastic strain is illustrated in Fig. 1. When the cumulative plastic strain value reaches the threshold ϵ_t , the cohesion decreases to the critical minimum value c_R .

$$c = c(\bar{\epsilon}_p) = c_0 + \kappa(\bar{\epsilon}_p) \quad (20)$$

The cumulative plastic strain is calculated using the following equation:

$$\dot{\bar{\epsilon}}_p = \dot{\lambda} \xi \quad (21)$$

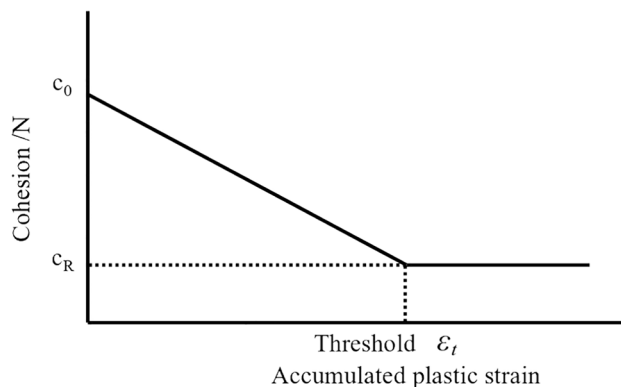


Fig. 1 Functional relationship between cohesion and cumulative plastic strain

$$\xi = \frac{6\cos\phi}{\sqrt{3}(3 - \sin\phi)} \tag{22}$$

This dynamic approach progressively decreases cohesion as plastic strain accumulates, thereby reflecting post-yielding damage and facilitating localized plastic flow. The variation of the cohesive softening function enables users to simulate material behaviors such as brittle fracture. However, it is challenging to obtain the pure mathematical relationship between cohesion and cumulative plastic strain, and it needs to be calibrated through the stress–strain relationship measured via uniaxial compression experiments.

4.2 Tensile Failure Model

This article applies the Grady Kipp model to describe the mechanical behavior of tensile failure (Melosh et al 1992; Gray and Monaghan 2004; Das and Cleary 2010). The two-parameter Weibull distribution model can describe the crack propagation process of internal defects in rocks under tension, as follows:

$$n = k\varepsilon^m \tag{23}$$

In the formula, n is the number of defects activated at the tensile strain level ε ; k and m are material constants that characterize fracture activation and have no direct physical significance.

The following equation can be used to describe damage growth, as proposed by Grady and Kipp (1980),

$$\frac{dD^{\frac{1}{3}}}{dt} = \frac{1}{3}c_g\alpha^{\frac{1}{3}}\varepsilon^{\frac{m}{3}} \tag{24}$$

$$\alpha = \frac{8\pi k(m + 3)^2}{(m + 1)(m + 2)} \tag{25}$$

Among them, D is the damage parameter, which varies between 0 and 1. $D = 1$ indicates that the particle has been completely damaged, while $D = 0$ indicates that the particle has not been damaged. c_g is the crack propagation speed, $c_g = 0.4 \times c_s$, where c_s is the velocity of sound in the material. In the equation, ε represents strain, which is a continuously changing quantity over time. The damage factor D can be calculated using time integration of the above equations.

4.3 Coupling of Grady–Kipp and Drucker–Prager

Deb and Pramanik first combined the Grady–Kipp model and the Drucker–Prager plasticity model within an SPH framework, and a comprehensive study of this process can be found in the work of Douillet-Grellier et al. In these

studies, scholars typically employ the Drucker–Prager model to describe shear failure, while the Grady–Kipp damage model is used to capture tensile failure. To better describe these two failure processes simultaneously, a combined damage factor D_{fa} is introduced and defined as follows:

$$D_{fa} = 1 - \frac{\bar{\varepsilon}_{pa}}{\max_{a \in \Omega}(\bar{\varepsilon}_{pa})} + D_a \tag{26}$$

where D_a represents the tensile damage factor of particle a , $\bar{\varepsilon}_{pa}$ represents the cumulative plastic strain value of particle a , and $\max_{a \in \Omega}(\bar{\varepsilon}_{pa})$ is the maximum cumulative plastic strain value taken.

In order to couple the two failure models, certain processing needs to be carried out in the algorithm:

If $F(I_1, J_2) \leq 0$ or $I_1 \geq 0$, the stress state is still elastic, so no plastic correction is required.

If $F(I_1, J_2) > 0$ and $I_1 < 0$, the stress state is in a plastic state, so plastic correction is required: $\sigma' = r^n \sigma$, $r^n = (-\alpha_\phi I_1^n + k_c) / \sqrt{J_2^n}$.

4.4 Implementation of the Contact Algorithm

In this study, the pressurized loading plates are considered as a rigid body that does not deform during rock compression. There is no interaction between the rock and the loading plates during the initial stage of motion. As shown in Fig. 2, once the loading plates are in close proximity to the rock particles, interactions between the rock particles and the loading plates occurs, and there are surface particles (such as particle k , particle $k + 1$) along the surface of the loading plate. These surface particles do not carry any material properties and are solely used to store the position information of the loading plates, facilitating the calculation of surface vectors and contact determination through particle search. The contact force between the rock and the loading plate consists of the vertical contact force and the horizontal contact force on the loading plate surface. The calculation formulae are as follows (Dong et al. 2016; Hu et al. 2023):

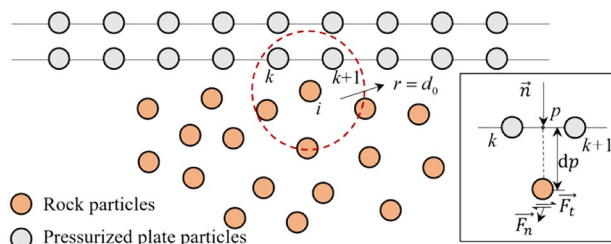


Fig. 2 Schematic diagram of the contact algorithm

$$\begin{cases} f_{ni} = (1 - \chi) \left[\frac{2m_i}{(\Delta t)^2} (d_0 - d_p) \right] \cdot n_p \\ f_{\tau i} = \mu |f_{ni}| \cdot \tau_p \end{cases} \quad (27)$$

In the formulae, χ represents the degree of penetration of the particles, μ is the coefficient of friction, τ_p and n_p represent the vertical and horizontal vectors formed by the two closest particle k and particle $k+1$ to the loading plate when the rock particles are subjected to the action of the loading plate. The expressions are:

$$\begin{cases} \tau_p = (t_x, t_y) = \left(\frac{x_{k+1} - x_k}{|x_{k+1} - x_k|}, \frac{y_{k+1} - y_k}{|x_{k+1} - x_k|} \right) \\ n_p = (-t_y, t_x) = \left(-\frac{y_{k+1} - y_k}{|x_{k+1} - x_k|}, \frac{x_{k+1} - x_k}{|x_{k+1} - x_k|} \right) \end{cases} \quad (28)$$

4.5 SPH Program Design

The program begins by initializing the parameters and the maximum number of calculation steps. If the current calculation step is less than or equal to the maximum, the program enters the main time integration loop. Within this loop, a single cycle is executed to calculate the soil internal force (including elastic and plastic stress components), artificial viscosity, artificial stress, XSPH correction, contact force between the soil and the loading

plate, and external force. Additionally, stress adjustments are performed. Finally, the diagonal components of the cohesion and stress tensor are updated based on the mixed failure algorithm. If the current calculation step exceeds the maximum, the program exits the main loop and outputs the results. The flowchart of the numerical simulation program is depicted in Fig. 3.

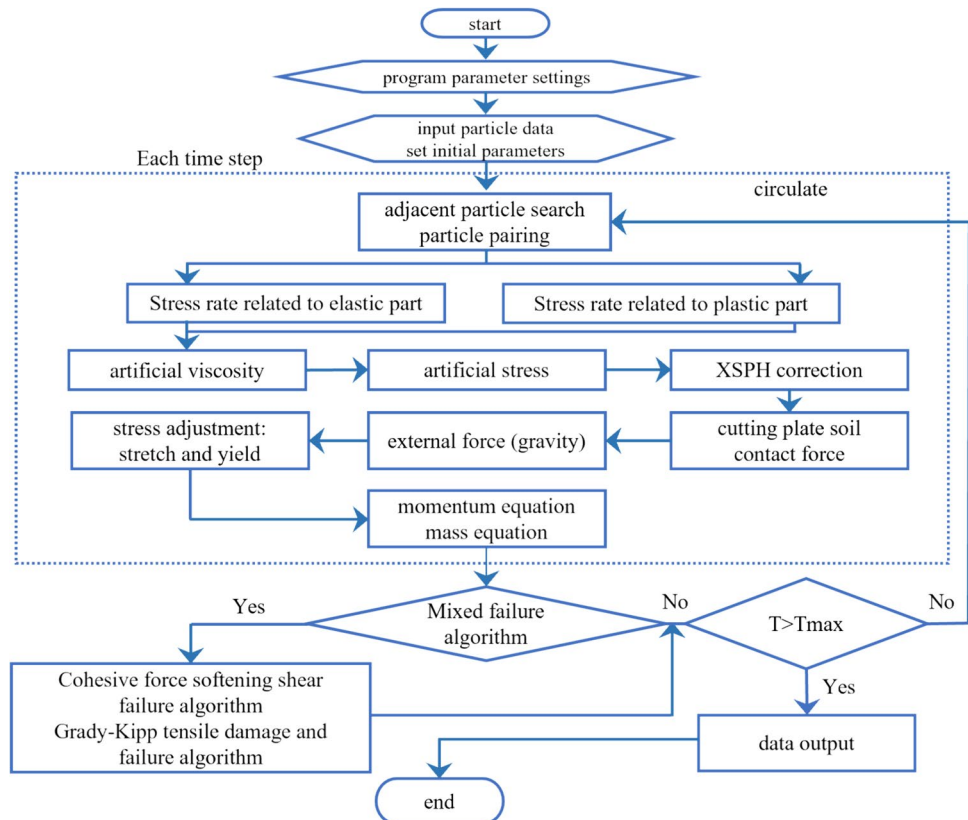
5 Numerical Examples and Test Verification

5.1 Crack Propagation in Rocks with Prefabricated Single Cracks Under Uniaxial Compression.

5.1.1 Model Establishment and Parameter Determination

In order to investigate the crack propagation and failure behavior of rock numerically and verify the model, a rock sample model containing a prefabricated crack was established in AutoCAD software and then imported into the program. As illustrated in Fig. 4, the dimensions of the rock sample are 50 mm × 100 mm, with a prefabricated crack of length 14 mm and width 2.0 mm located in the center. The upper and lower loading plates are geometrically symmetrical, with the lower plate fixed and the upper plate moving downward at a velocity of 0.2 m/s. To

Fig. 3 Numerical simulation program flowchart



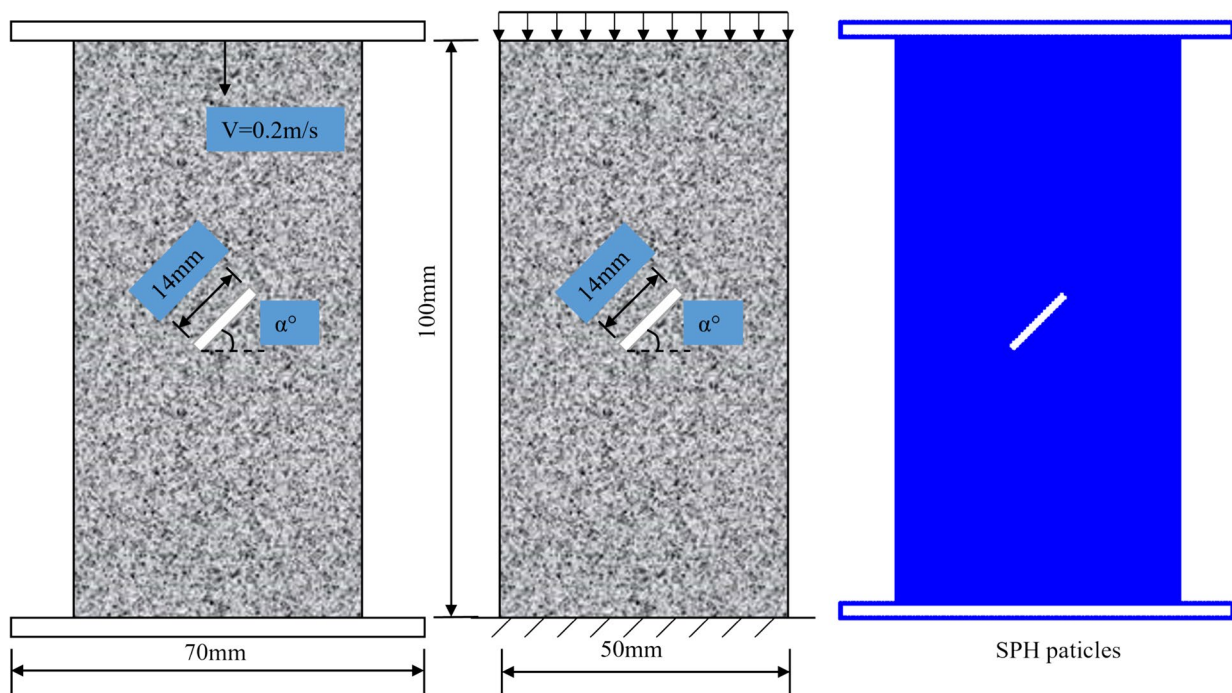


Fig. 4 Schematic diagram of physical models of rock samples and loading plates

Table 1 Material parameters

Parameter	Numerical	Experimental (by Yang shengqi)
Dimension/(mm × mm)	50 × 100	50 × 100
Density/(kg/m ³)	2410	2410
Elastic modulus/GPa	5.96	6
Bulk modulus/GPa	3.31	3.3
Shear modulus/GPa	2.5	2.5
Poisson's ratio	0.2	0.2
Cohesion/MPa	15	15
Friction angle/°	45	45

represent realistic material behavior the rock parameters are assigned based on values from Yang's experiments, as detailed in Table 1.

5.1.2 Center-Inclined Crack Propagation Under Uniaxial Compression

Figure 5 illustrates the fracturing process of a sandstone sample containing a 45° prefabricated flaw under uniaxial compression. It can be observed that new tensile cracks first generate at both tips of the original flaw and gradually expand. Subsequently, as the loading plate continues moving, new secondary shear cracks simultaneously appear at

the crack tips. Notably, new tensile cracks propagating along the axial stress direction also initiate on the shear crack surface. These observations demonstrate that the mixed failure model can effectively simulate the formation of both tensile and shear cracks arising from the flaw-induced stress concentrations under uniaxial compression. To clarify crack types, Bobet and Einstein (1998) proposed the following crack classifications in their rock mechanics studies: Shear wing crack: Induced by compressive stress, extending at an angle from the defect tip. Secondary tensile crack: Driven by tensile stress, propagating perpendicular to the principal stress direction. Bridge shear crack: Forming between two defects, leading to rock splitting. To further clarify and categorize the various crack types observed during the fracturing process, Yang et al. (2022) summarized the types of cracks in order to systematically evaluate the cracking behavior of specimens containing flaws, including the following: Crack type T_w : Initiation from the tip of a prefabricated crack, gradually extending towards the specimen boundary along the axial stress direction. Crack type T_s : Originating after T_w , it propagates from the crack tip towards the axial stress direction. Crack type T_t : A tensile crack that initiates on the shear crack surface. Crack type S_m : The main shear crack starts at the tip of the prefabricated crack, and the direction of crack propagation is similar to that of the prefabricated crack.

Figure 6a illustrates the types of crack propagation cracks in rock samples under uniaxial compression, including shear

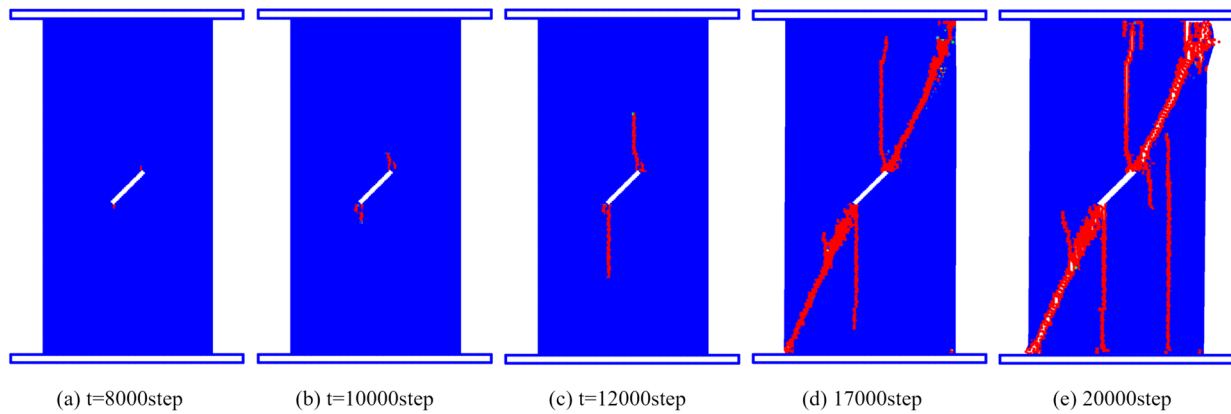
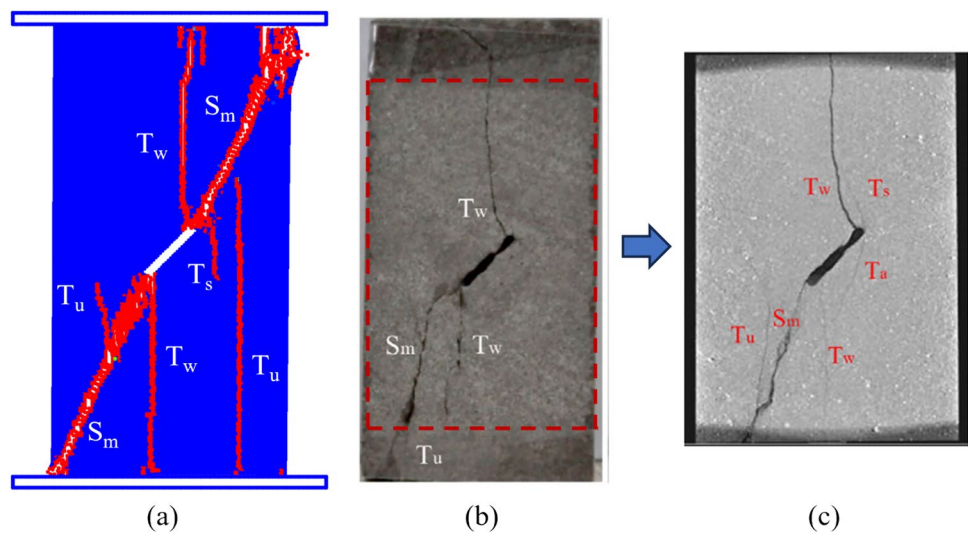


Fig. 5 Simulation results of crack propagation under uniaxial compression using a mixed failure model

Fig. 6 Schematic diagram of crack types during uniaxial compression of rocks. **(a)** Simulation results; **(b)** Experimental failed specimen (Yang et al. 2022); **(c)** Surface CT image of failed specimen in the range of scanning region (Yang et al. 2022)



cracks and tensile cracks. It was observed that shear cracks propagate in the direction of maximum shear stress, while tensile cracks initiate perpendicular to the loading direction, caused by tensile stress concentrations at structural discontinuities. Figure 6b, c show the experimental results and surface CT image, respectively, of a failed specimen in the range of the scanning region. The experimental result in Fig. 6b reveals the major macroscopic shear and tensile fractures, along with fragmentation of the rock sample after failure. Figure 6c offers a detailed microscopic view of the crack propagation captured through CT imaging. They both comprehensively illustrate the mixed-mode fracture process in the tested rock sample under uniaxial compression, validating the capability of the numerical model to describe the complex crack evolution associated with mixed-mode rock failure under compression

Notably, the complex structure and heterogeneous nature of rocks can indeed lead to dispersion or variability in experimental test results, even under seemingly identical

loading conditions. This inherent complexity arises from the presence of micro-structural features, such as pores, inclusions, pre-existing microcracks, and compositional variations, which are randomly distributed and oriented within the rock matrix. This intrinsic complexity poses significant challenges in accurately simulating the precise location and propagation of cracks within numerical models. However, despite the challenges in replicating the precise crack patterns, the numerical simulations have the potential to predict and capture the overall crack propagation and post-peak behavior of the rock samples with reasonable accuracy, which provide valuable insights into the macroscopic response of the rock under compressive loading, including the onset of yielding, peak strength, and the post-peak softening behavior.

Additionally, the current simulations adopt a two-dimensional modeling approach under the assumption of plane strain conditions. While this simplification provides computational efficiency and valuable insights into the fracture

processes, it inherently introduces limitations in representing the full three-dimensional nature of crack growth and coalescence. It may influence factors such as out-of-plane deformations, mixed-mode fracture interactions, and confinement effects, potentially deviating from the behavior observed in unconfined 3D specimens.

5.1.3 Comparative Analysis of SPH Simulations and Experimental Findings with Varying Flaw Orientations

To comprehensively evaluate the mixed-mode failure model and its ability to capture the complex fracture behavior of rocks, we conducted numerical analysis on rectangular cross-section rock samples with an aspect ratio of 2.0. Each sample contained prefabricated flaws of a certain width, oriented at angles of 0° , 30° , 45° , 60° , and 75° to the loading direction, respectively. This range of flaw orientations allowed us to investigate the influence of flaw geometry on the fracture response under uniaxial compression.

For samples with 0° oriented defects (flaws perpendicular to the loading direction), the simulation process revealed that when the failure strength was reached, several inclined secondary cracks initiated at the end or middle of the pre-existing flaw. These secondary cracks rapidly expanded towards the exterior of the sample, facilitated by the high stress concentrations at the flaw tips. The propagation of these secondary cracks resulted in shear sliding along the newly formed fracture planes, ultimately leading to overall shear failure of the sample. Notably, a tensile crack appears in the center of the 0° flaw, prior to any microcracking at the flaw tips. This early tensile crack is indicative of the localized tensile stress concentration zone within the flaw center, driven by the applied compressive loading. Similarly, for samples with 30° and 45° inclined flaws, the simulations capture the initiation and opening of wing tensile cracks at the flaw tips before the onset of shear failure. As the wing cracks extended under increasing load, shear cracks nucleate from the flaw tips and propagate rapidly across the samples, eventually leading to complete shear failure along the pre-crack plane. In contrast, when the inclination direction of the flaw is close to the axial direction (60° , 75°), the simulation results show the formation of only one main crack around the prefabricated flaw. Significant secondary cracks or wing cracks are absent for these steeply inclined flaws, suggesting a different fracture mechanism influenced by the flaw orientation.

Table 2 presents complete simulation results of rock samples with varying flaw inclination angles under uniaxial compression loading. The table includes the morphological progression of cracking, displacements, and stress distributions. These simulations are compared with the experimental works conducted by Yang, Cheng and Jiang, and the

numerical results exhibit good correspondence with experimental observations, validating the predictive capabilities of the model.

The observed fracture patterns can be attributed to the stress state and mechanisms within the rock under uniaxial compression loading. Rocks are subjected to compressive stress perpendicular to the loading direction, leading to the formation of a major stress field inside the rock matrix. When cracks or flaws are present, local stress concentrations arise around these discontinuities, potentially causing an increase in stress at the crack tips and promoting crack propagation. Furthermore, for rocks with preexisting cracks, deformation around these discontinuities can lead to a non-uniform distribution of strain fields within the material. Consequently, strain tends to concentrate at the crack tips, further aiding crack propagation. During this process, strain concentration also occurs at the crack tip, subjecting the region to additional stress and further promoting crack growth. The path of crack propagation typically advances along the direction of high stress concentration or weak planes within the rock matrix.

Notably, despite the inherent symmetry of this case ($\alpha=0^\circ$), the sample displays an asymmetric failure pattern. While slight material inhomogeneities can account for the lack of symmetry in physical experiments, these simulations involve a perfectly homogeneous material. The preferred fracture orientation observed in this model likely stems from a lack of symmetry in the discretization scheme relative to the geometry.

In order to further validate the efficacy of the mixed-mode failure model in capturing the intricate fracture behavior of rocks, Fig. 7 presents the detailed simulated stress–strain response for a sandstone sample subjected to uniaxial compressive loading. The simulated curve exhibits several distinct and abrupt stress drops, which correspond to the initiation of cracks emanating from the tip of the prefabricated flaws within the sample. There crack initiation ultimately leads to a rapid and significant loss of bearing capacity, culminating in the complete failure of the rock sample.

The loading characteristics of uniaxial compression experiments on rocks are typically characterized by a stress–strain curve exhibiting five stages. Stage I involves microfractures and pore compaction, leading to nonlinear deformation as cracks and pores close under the compressive stress. Stage II is marked by an approximately linear elastic behavior as the pores within the rock matrix stabilize and the rock material responds elastically to the increasing load. As the loading progresses, Stage III commences, during which existing cracks extend and new cracks initiate in a relatively stable propagation regime. Stage IV signals the onset of accelerated and unstable crack growth, marking the transition from elastic to inelastic (plastic) deformation within the rock. Finally, Stage V is characterized by a sudden

Table 2 Simulation results and experimental comparison of uniaxial compression of rocks with single prefabricated cracks

	Crack growth	Displacement/m	Stress distribute/MPa	Experimenta l result in Yang(Yang <i>et al.</i> , 2022)	Experimental result in Cheng(Chen <i>g et al.</i> , 2018)	Experimenta l result in Jiang(Jiang <i>et al.</i> , 2019)
(a) $\alpha=0^\circ$						
(b) $\alpha=30^\circ$						
(c) $\alpha=45^\circ$						
(d) $\alpha=60^\circ$						
(e) $\alpha=75^\circ$						

and significant stress drop, indicative of the extensive crack interconnection and the ultimate failure of the rock sample. The stress–strain curve can demonstrate the progressive fracturing process within the rock sample, with each stage of deformation correlated to specific fracture mechanisms and crack evolution patterns. As observed in Fig. 7, the simulated stress–strain curve exhibits substantial stress drops even before reaching the peak strength. These stress drops can be attributed to several key fracture events occurring within the sample. The initiation and expansion of micro

cracks inside the rock sample (Stage I), macroscopic fracture on the surface of the rock sample (Stage III), and sliding and dislocation of the rock sample structure (Stage IV), involving the sliding of crack surfaces, rearrangement of grain contacts and strength loss (Stage V). In summary, the simulated stress–strain response demonstrates the progressive crack evolution corresponding to each stage of deformation and failure within the rock sample. The mixed-mode fracture model successfully captures the complete stress–strain response, including the distinct stress drops and complex

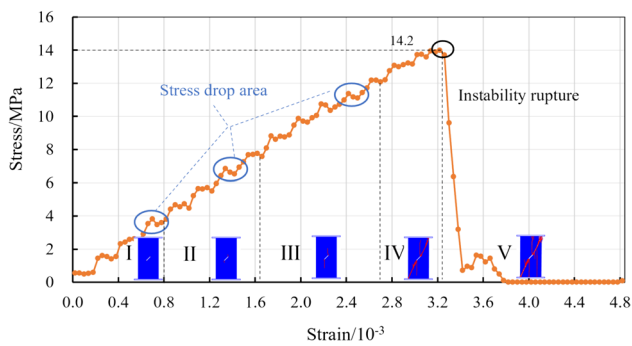


Fig. 7 Stress–strain curve of rock under uniaxial compression

cracking processes observed experimentally. It validates the capabilities for simulating damage and failure in brittle rock materials, replicating the intricate fracture mechanisms and deformation behavior under compressive loading conditions.

Figure 8 compares the simulated stress–strain curve to experimental curves obtained by Yang and Cheng. From a qualitative standpoint, the behavior of the model closely resembles that of the experiments. However, there are some quantitative discrepancies in the absolute values. Specifically, fractures in the SPH model occur at much lower loads compared to the experiments. This same phenomenon, where the model predicts fracture at lower loads than experiments, was also reported by Douillet-Grellier when applying the model to uniaxial compression of a gypsum sample containing an angled flaw. One potential reason for this discrepancy is that in the simulations, failure is detected before an actual fracture aperture opens up, whereas in experiments fracture initiation is only visually evident after the aperture opens.

Other two aspects may contribute to the observed differences between the simulation results and experimental data. Firstly, the material modeled in the SPH simulations is considered homogeneous and isotropic, which is not representative of the inherent heterogeneity and anisotropy present in real rock specimens used in experiments. Additionally, the loading rate employed in these simulations (0.2 m/s) is not consistent with the loading rates typically used in the original experiments (4 MPa/min), which could influence the fracture behavior. Secondly, the SPH simulations are conducted in a two-dimensional framework, assuming plane strain conditions, whereas the experiments are performed on three-dimensional specimens with a finite width of 50 mm, which violates the plane strain assumption. This geometric simplification in the simulations may lead to discrepancies in the fracture patterns observed. Qualitatively, the behavior exhibited by the numerical model and the experiments are remarkably similar, capturing the essential fracture mechanisms.

Furthermore, in Douillet-Grellier's work, the tensile wing cracks are oriented towards the corners of the sample in SPH simulations, while they are directed vertically towards the top boundary of the specimen in experiments. This deviation can be attributed to the no-slip boundary condition imposed at the loading plate boundary in the SPH model, which limits the development of vertical tensile cracks and causes them to deviate towards the corners. According to the SPH simulations in this study, the tensile wing cracks are successfully captured with the help of the contact algorithms at the interface of the loading plate and rock specimen. This improvement in dealing with the interaction between the specimen and the loading plate better represents the actual experimental conditions.

5.2 Crack Propagation in Rocks with Prefabricated Double Cracks Under Uniaxial Compression

To further validate the robustness and versatility of the mixed-mode failure model, numerical simulations of uniaxial compression are performed on rock samples containing two prefabricated flaws. Based on the spatial arrangement and orientations of the double flaws, three model configurations are analyzed, as illustrated in Figs. 9, 10. Table 3 presents the simulation results for the three models, including the crack propagation morphology, displacement fields, and stress distributions under uniaxial loading conditions for model (a), model (b), and model (c). As shown in the crack evolution sequences in Fig. 8, crack initiation emanates abruptly from the tips of the prefabricated flaws due to the localized stress concentrations introduced by the applied compressive loading. As the loading continues, the initiated cracks propagate steadily towards each other, driven by the increasing stress intensity at the crack tips. Upon interaction and intersection of the propagating cracks, a continuous fracture path is established, fully penetrating the rock specimens. This interconnected cracking network ultimately precipitates complete failure of the samples via shear sliding along the newly formed fracture planes. Notably, the specific failure patterns and crack coalescence mechanisms depend on the spatial arrangement and orientations of the prefabricated flaws.

For the rock sample of the geometric model (a) configuration, the crack initiation proceeds from the outer tip of the prefabricated flaws, propagating vertically under the increasing compressive load. As the vertical cracks extend towards the sample surface, wing cracks also initiate from the inner precrack tips, driven by the localized tensile stress concentrations. With continued loading, these wing cracks expand and coalesce with the vertical cracks, forming macroscopic fractures that effectively separate the sample into discrete sections. Ultimately, the progressive growth and intersection

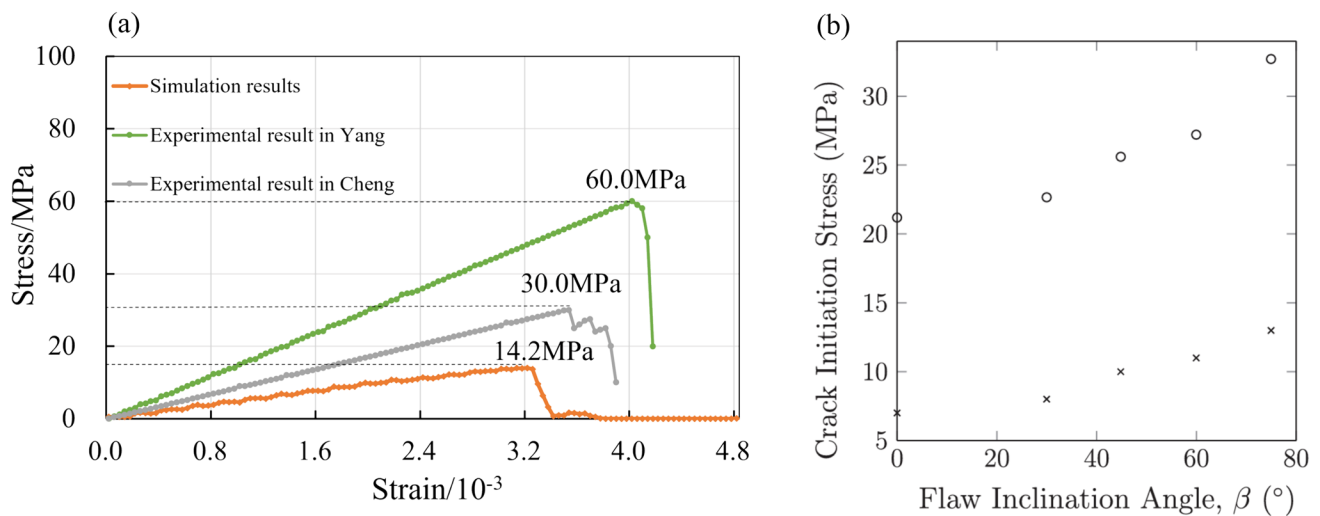


Fig. 8 (a) Comparison of stress–strain curves (b) Absolute values of stress at moment of observed fracture initiation, SPH results (×) and experimental data (o) when fracture opening is observed (Wong)

of multiple cracks emanating from the tips of the double precracks leads to complete fragmentation of the specimen.

For the rock sample of geometric model (b), the fracturing process commences with cracks initiating from the tips of both prefabricated flaws, propagating normal to the preflaw planes. As the load increases, the cracks gradually rotate to vertical orientations. Subsequently, the cracks begin to develop and penetrate from the outer tips of the two prefabricated flaws towards the two corners of the specimen,

eventually leading to complete failure of the geometry (b) sample.

For the rock sample of geometric model (c), the fracturing sequence initiates with the connection of the inner tips of the two prefabricated cracks. Subsequently, vertical cracks initiate from the outer precrack tips and propagate upwards as the load increases. Continued loading leads to the growth of oblique crack from the outer tips towards the sample corners. Ultimately, the coalescence of the inner cracks, combined with the propagation and intersection of

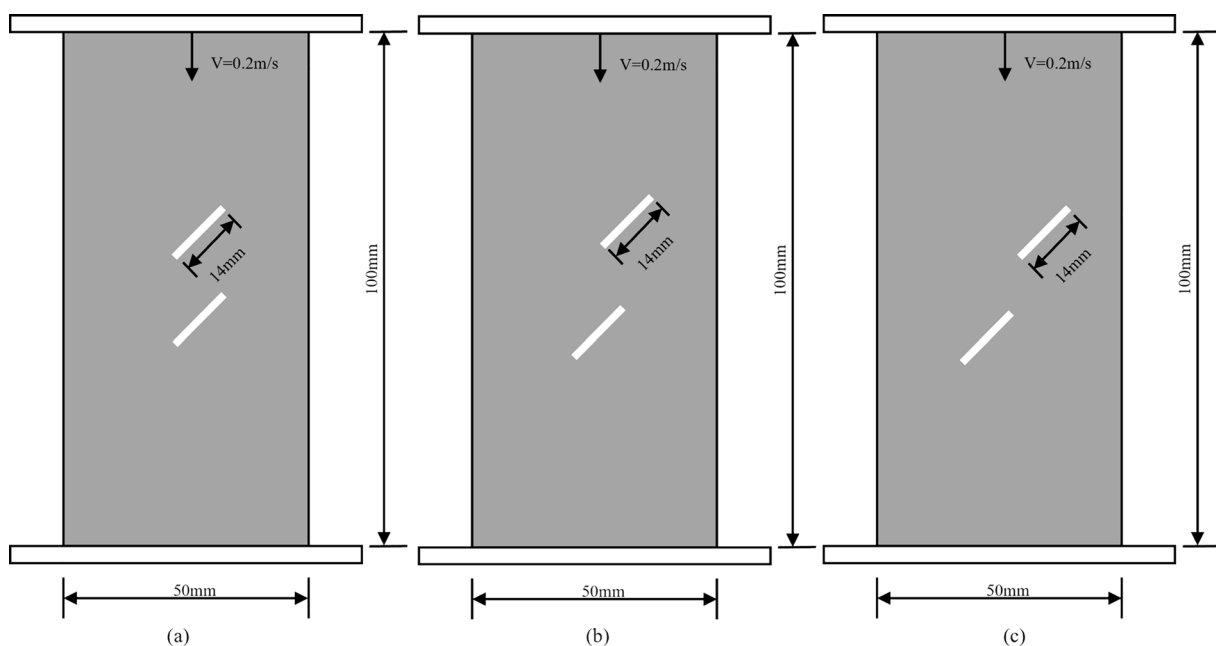


Fig. 9 The geometric model of a rock sample with two pre-existing flaws

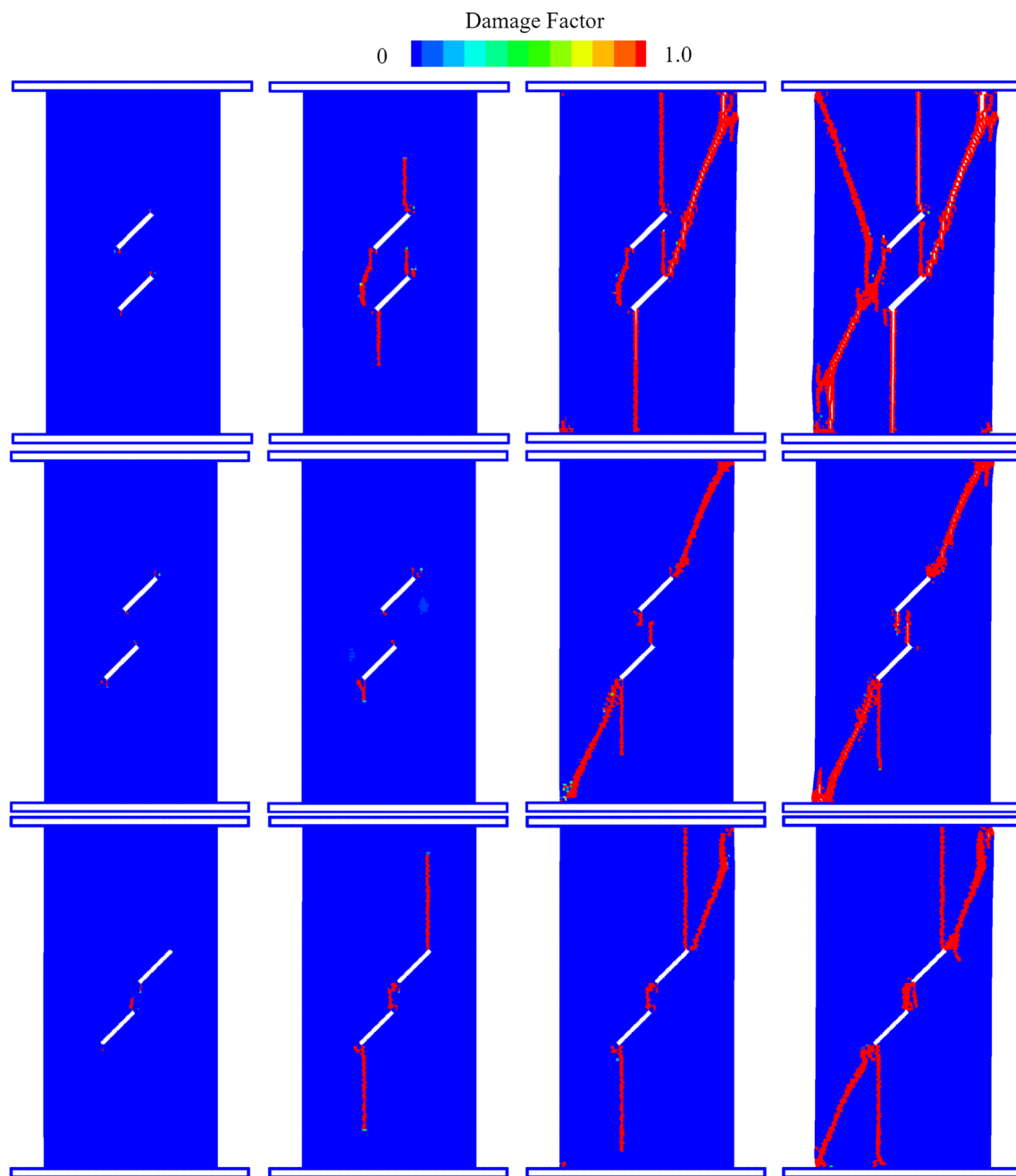


Fig. 10 Crack propagation in three prefabricated double-crack rock specimens with varying distributions under uniaxial compression

the outer vertical and oblique cracks, permeates the entire geometry (c) specimen, culminating in gross failure.

These modeling results show good agreement with the experimental measurements reported by Li (2015) on pre-cracked specimens subjected to uniaxial compression. The verification demonstrates the capability of the mixed-mode fracture model to capture the complex interactions between multiple cracks and simulate the complete failure process under compressive loading conditions, irrespective of the flaw geometries and arrangements.

6 Results and Discussions

This section presents an analysis and discussion of the numerical experiments conducted to investigate the crack propagation behavior and failure mechanisms of rocks under uniaxial compression loading. By analyzing factors such as pre-flaw lengths, cohesion, friction coefficients of loading plates, and it not only enhances the robustness of the model but also provides valuable insights into the sensitivity of the response to various input parameters. This

Table 3 Simulation results and experimental comparison of uniaxial compression of rocks containing two pre-existing flaws

	Crack growth	Displacement/mm	Stress distribute/MPa	Experimental result (Li, 2015)
Model(a)				
Model(b)				
Model(c)				

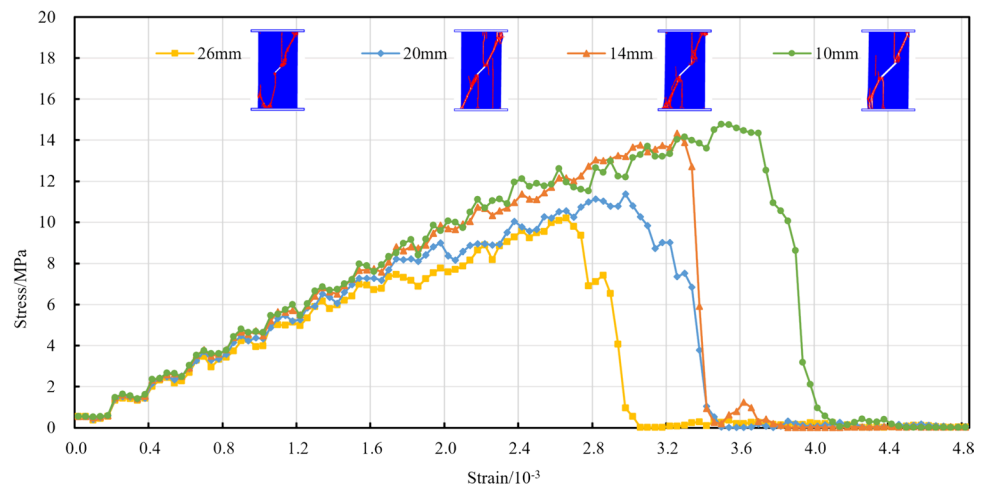
analysis facilitates a better understanding of the model and the underlying mechanisms governing the damage evolution process.

6.1 Influence of the Prefabricated Flaw Length

To assess the impact of prefabricated flaw length on the mechanical response of rock samples, uniaxial compression simulations are conducted on samples containing angled pre-existing flaws oriented at 45 degrees, with

lengths varying from 10 to 26 mm, specifically at 10 mm, 14 mm, 20 mm, and 26 mm. Figure 11 presents the complete stress–strain curves obtained from these simulations for the rock specimens with different flaw lengths subjected to uniaxial compression loading. It is evident that an increase in the angled flaw length leads to a weakening effect, resulting in a reduction of the peak strength exhibited by the rock samples. Figure 12 shows the relationship between crack length and the corresponding peak strength values extracted from the stress–strain curves. A

Fig. 11 Stress–strain curve of prefabricated fractured rocks with a 45° inclination and varying lengths



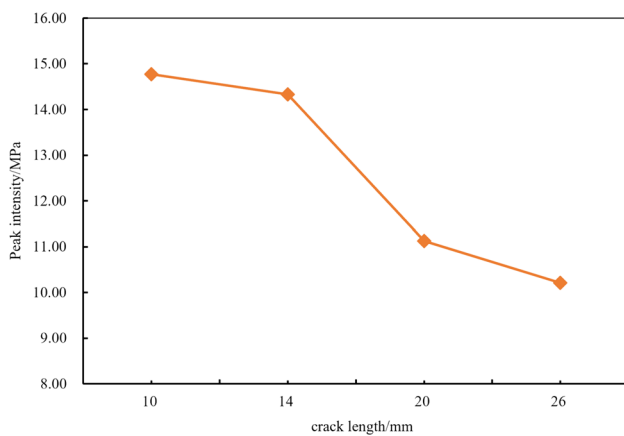


Fig. 12 The relationship between crack length and peak strength

decreasing trend in peak strength can be observed as the crack length increases, which is consistent with experimental observations reported in the literature (Wang 2018).

6.2 Influence of the Cohesive Force Softening Relationship

Determining the relationship between cohesion and accumulated plastic strain is a challenging task in laboratory measurements, as it is a purely mathematical construct rather than a directly measurable physical parameter. In addition, by changing the mathematical form of the cohesive softening relationship, a wide range of material behaviors including brittle and ductile materials, can be simulated. More complex strength models can be achieved by incorporating higher order equations to describe the evolution of cohesion with accumulated plastic strain. In this study, the cohesion

softening relationship description incorporates three key factors: the overall cohesive strength, the softening curve describing cohesion degradation with accumulated damage, and the damage threshold at which softening is triggered. By independently varying each parameter while holding the others constant, four numerical case studies are conducted to investigate the influence of the cohesive softening relationship parameters on the crack propagation morphology, as summarized in Tables 4, 5, 6, 7.

The results demonstrate that while the angle of the pre-fabricated flaw remains unchanged, the final shape of crack propagation changes significantly with variations in the cohesive force. Furthermore, when the cohesion remains unchanged, the angle of the prefabricated flaw has a significant impact on the crack propagation morphology. Interestingly, when the cohesion remains constant and the pre-crack angle is 30° , the threshold in the cohesion softening relationship has little effect on the crack propagation morphology, and the crack propagation direction and angle are almost consistent. However, when the cohesion remains constant and the crack initiation angle is 0° , the threshold has a significant impact on the crack propagation morphology. It is evident that the cohesive force, threshold, and angle of prefabricated flaws all affect the final morphology of crack propagation, but the impact of the threshold on crack propagation does not follow a specific pattern.

In summary, the cohesive strength, softening relationship, and pre-existing flaw orientation collectively affect the final crack morphology. These findings provide valuable guidance for calibrating cohesive models to achieve realistic simulation of fracture behaviors in rock materials.

Table 4 Prefabricated crack angle of 30° , results of different thresholds and cohesions

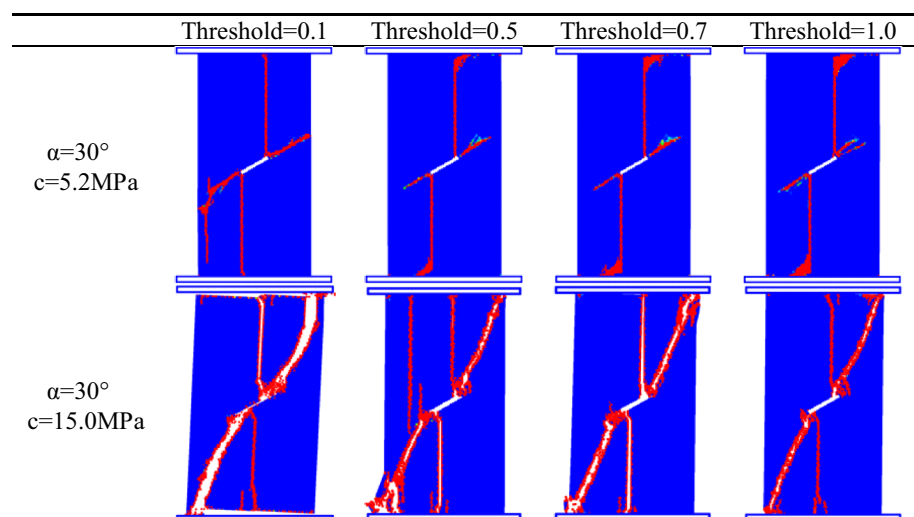


Table 5 Prefabricated crack angle of 0° , results of different thresholds and cohesions

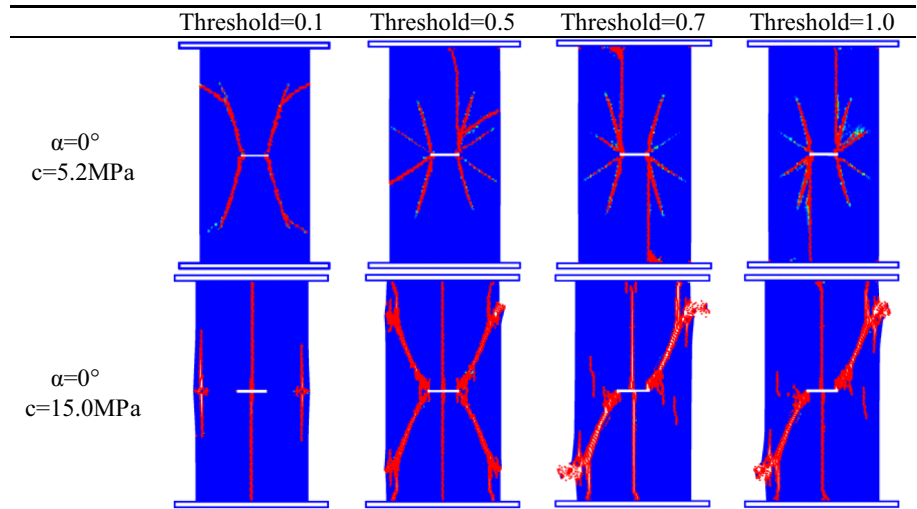


Table 6 Cohesive force of 5.2 MPa, results of different thresholds and pre crack angles

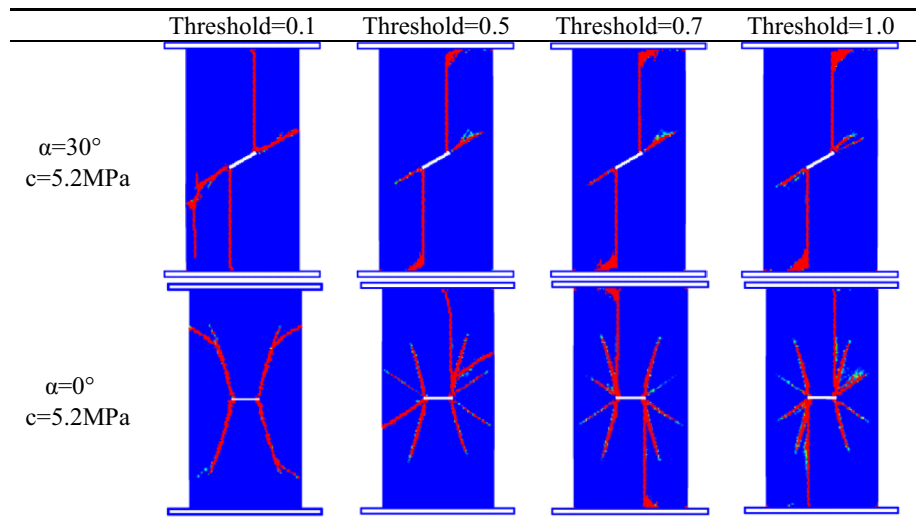
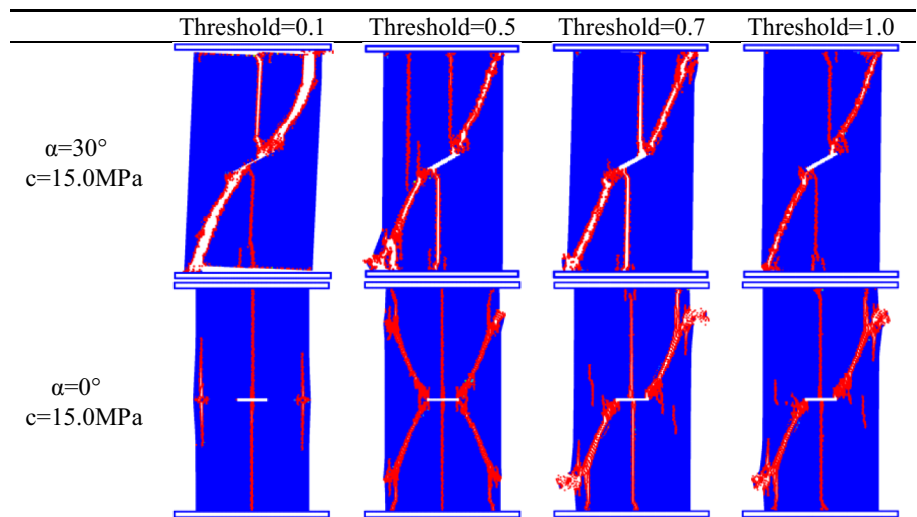


Table 7 Cohesive force of 15.0 MPa, results of different thresholds and pre crack angles



6.3 Influence of the Friction Coefficient on Loading Plates

The friction coefficient at the interface between the loading plate and the specimen has a significant influence on the peak strength observed in the stress–strain curve, as evidenced in Fig. 13. When the friction coefficient μ is varied from 0.1 to 0.9, a decreasing trend in peak strength under uniaxial compression is observed. This reduction in strength with increasing friction can be attributed to two main aspects. Firstly, an increase in the friction between the loading plate and the sample results in a more uneven stress distribution between cracks within the specimen, leading to the early development and expansion of cracks. Consequently, this reduces the compressive strength of the sample, and therefore, the peak strength observed in the compression test decreases accordingly. Secondly, higher friction restricts the lateral deformation ability of the rock in the loading direction, increasing the brittleness of the sample and further contributing to the reduction in the peak strength.

The change in the friction coefficient of the loading plate also has a certain impact on the elastic stage of the stress–strain curve. In the initial stage, due to the relatively small stress value, the difference between the four sets of data is not significant. However, as the strain increases, the stress values diverge, reflecting the influence of the friction coefficient. Interestingly, from the inset images depicting crack propagation, it can be observed that the friction coefficient has little effect on the morphology of crack propagation. This suggests that while the friction coefficient influences the overall strength and stress–strain response, it does not significantly alter the fracture patterns or crack propagation paths within the specimens. Qi et al. (2021) also pointed out that as the friction coefficient increases, the axial stress increases, and the failure of the specimen occurs later.

These findings underscore the importance of accurately characterizing and accounting for the friction coefficient at

the loading plate–specimen interface in numerical simulations and experiments involving rock compression. Appropriate measures, such as the use of friction-reducing materials or lubricants, may be necessary to minimize the influence of friction and obtain more representative results reflecting the intrinsic material behavior.

6.4 Influence of Different Values of Cohesion

The strength of the cohesive force representing interparticle bonding mainly affects the strength of the rock. As illustrated in Fig. 14, in the initial elastic deformation regime, the cohesion has no impact on the Young's modulus of the rock sample. However, the peak strength exhibits an increasing trend as the cohesive bonds between particles become stronger.

At the micro-scale level, this behavior can be attributed to the fact that greater cohesion between particles impedes their ability to slide and move relative to one another, thereby requiring a larger force for bond failure and particle separation to occur. Consequently, higher peak strengths are observed for rock samples with stronger cohesive bonds between the constituent particles. While cohesive strength plays a negligible role in governing the elastic properties, it is an important factor in controlling the transition from elastic to plastic deformation and the ultimate strength limits according to the model employed in this study. Therefore, the cohesion parameter strongly influences the peak strength but does not affect the initial elastic response, and calibration of cohesion parameters is crucial for replicating failure modes in rocks. By carefully using the cohesion parameter to the model can provide reliable predictions of the mechanical behavior and fracture processes in rocks under various loading conditions.

Fig. 13 The Influence of Friction Coefficient of Pressurized Plate on the stress–strain Curve of Rock under Uniaxial Compression

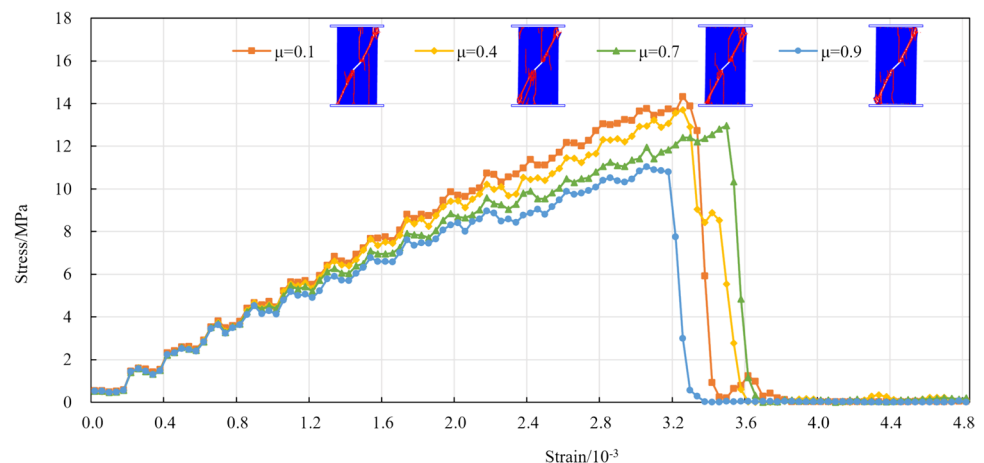


Fig. 14 The Effect of Cohesion on the stress–strain Curve of Rock during Uniaxial Compression

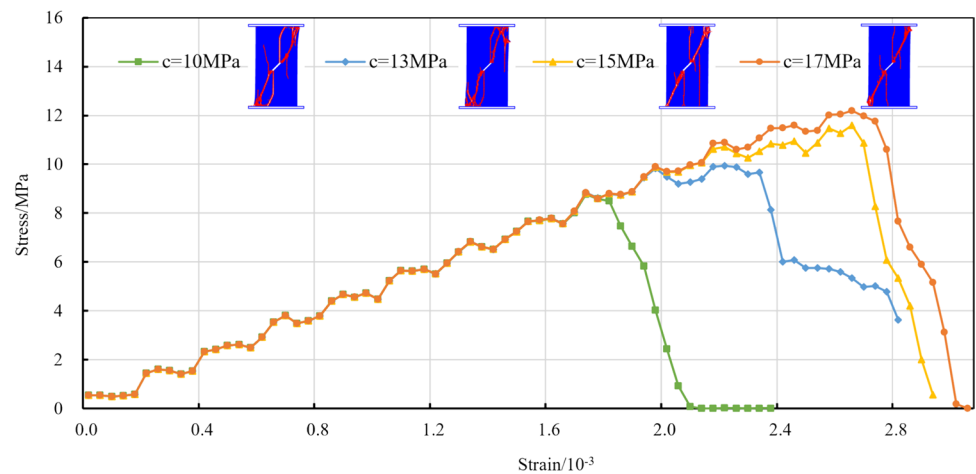
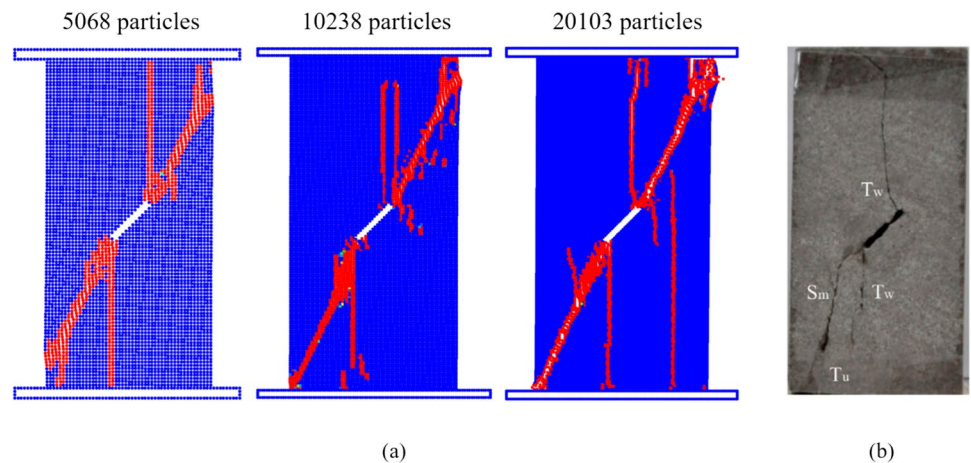


Fig. 15 Final failure modes of rock samples with a prefabricated flaw under uniaxial compression with different particle numbers. (a) Numerical results; (b) Experimental results (Yang et al. 2022)



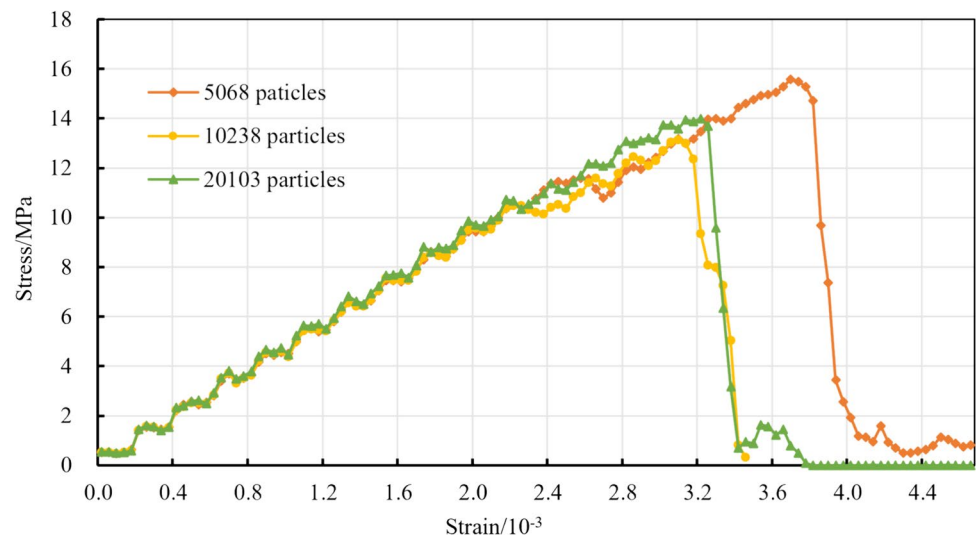
6.5 Influence of the Particle Count

The particle discretization, including the number of particles and particle spacing, is an important modeling consideration that influences the computational accuracy and simulated crack propagation patterns., as shown in Figs. 15 and 16. Figure 15 compares the final failure morphologies of preflawed rock samples with a 45° inclination angle under uniaxial compression using different particle resolutions. While the overall crack propagation mode and trajectory appear similar across the cases, some variations are evident depending on the number of particles representing the sample microstructure. It can be observed that finer resolutions better capture the material heterogeneity and provide more potential crack propagation pathways.

Figure 16 shows the stress–strain curves of rock samples with different particle numbers under uniaxial compression. The elastic regime, minimal variation in Young's modulus is observed with changing particle number, indicating that adequate bulk stiffness is achieved even with reduced resolution. However, the peak strength demonstrates greater sensitivity

to the particle discretization. Notably, the model with 5,068 particles produces an anomalously high strength compared to the finer resolutions, implying that an inadequate number of particles fails to properly simulate the progressive microfracturing and coalescence controlling failure. In comparison with experimental results, the model with 20,103 particles and a 0.5 mm spacing, used in this study, provides a suitable accuracy for the specimen size. A minimum level of discretization is required to capture the correct material behavior and fracture processes accurately. Proper calibration of particle resolution relative to specimen geometry and loading conditions is essential to produce realistic simulations. These findings highlight the importance of carefully selecting the particle discretization scheme in numerical simulations of rock fracture. While coarser resolutions may be computationally more efficient, they may fail to capture the intricate fracture processes and lead to inaccurate predictions of strength and failure behavior. Conversely, excessively fine resolutions may be computationally expensive without providing significant improvements in accuracy. A balanced particle count and particle resolution, informed by

Fig. 16 Stress–strain curves of rock models with different Particle number under uniaxial compression



convergence studies and experimental validation, is recommended to optimize the particle discretization for the specific problem.

7 Conclusion

This study investigates a coupled damage model integrating the Drucker–Prager and Grady–Kipp criteria within a smoothed particle hydrodynamics (SPH) framework. The mixed-mode failure model enables the simulation of complex crack initiation and propagation in flawed rocks under uniaxial compression loading condition. The model is validated through comparisons with experimental observations of single and double pre-cracked specimens. The numerical analyses successfully capture the morphology and interactions of mixed tensile and shear fracturing leading to complete sample failure. The simulated stress–strain curves exhibit the characteristic progressive fracturing corresponding to different deformation mechanisms observed experimentally. Comprehensive parametric studies are conducted to investigate the governing factors influencing the model predictions. The results indicate that pre-crack geometry, cohesion, friction at the loading plate, and particle discretization resolutions can significantly impact the simulated cracking modes, peak strength, and post-failure response. However, certain parameters, such as the damage threshold, demonstrate situational dependence based on the specific cracking scenarios considered. The approach provides an advanced tool for investigating crack initiation and propagation induced by flaws under compression loading in rock materials. Further refinement of the model through additional experimental validation and calibration could enhance realism of predictions for failure mechanisms in geological materials across a broader

range of conditions. Overall, this study contributes to a deeper understanding of the complex fracture processes in flawed rock specimens and demonstrates the potential of coupled damage model and SPH techniques for accurate simulations of fracture phenomena in geological and geomechanical applications.

Acknowledgements The authors want to thank the support of the Sichuan Province key research and development project (No.2023YFS0438), Technology Support Program Project of Guizhou Province (Grant No. [2021] General 341) and Innovation Research 2035 Pilot Plan of Southwest University(SWU-XDPY22003).

Author Contributions All authors contributed to the study conception and design. Supervision, Project administration, Funding acquisition and Formal analysis were performed by Man Hu. The first draft of the manuscript was written by Qiuting Tan and all authors commented on previous versions of the manuscript. Coding and Data curation were performed by Qiuting Tan. Software and Resources were performed by Dianlei Feng and Yi Ren. Supervision was performed by Yu Huang. All authors read and approved the final manuscript.

Funding The authors are grateful to Sichuan Province key research and development project via a project: No. 2023YFS0438, Technology Support Program Project of Guizhou Province via a project: Grant No. [2021] General 341, Innovation Research 2035 Pilot Plan of Southwest University via a project: SWU-XDPY22003.

Data Availability The related data used to support the findings of this study are included within the article.

Declarations

Conflict of interest The authors declare that they have no known competing financial interests or personal relationships that could have appeared to influence the work reported in this paper.

References

- Ambati M, Gerasimov T, De Lorenzis L (2015) A review on phase-field models of brittle fracture and a new fast hybrid formulation. *Comput Mech* 55(2):383–405. <https://doi.org/10.1007/s00466-014-1109-y>
- An HM et al (2017) Hybrid finite-discrete element modelling of dynamic fracture and resultant fragment casting and muck-piling by rock blast. *Comput Geotech* 81:322–345. <https://doi.org/10.1016/j.compgeo.2016.09.007>
- Bleyer J, Alessi R (2018) Phase-field modeling of anisotropic brittle fracture including several damage mechanisms. *Comput Method Appl M* 336:213–236. <https://doi.org/10.1016/j.cma.2018.03.012>
- Bonilla-Sierra V et al (2015) Rock slope stability analysis using photogrammetric data and DFN-DEM modelling. *Acta Geotech* 10(4):497–511. <https://doi.org/10.1007/s11440-015-0374-z>
- Bui HH, Fukagawa R (2013) An improved SPH method for saturated soils and its application to investigate the mechanisms of embankment failure: case of hydrostatic pore-water pressure. *Int J Numer Anal Methods Geomech* 37(1):31–50
- Bui HH, Sako K, Fukagawa R (2007) Numerical simulation of soil-water interaction using smoothed particle hydrodynamics (SPH) method. *J Terramech* 44(5):339–346
- Bui HH, Fukagawa R, Sako K, Ohno S (2008) Lagrangian meshfree particles method (SPH) for large deformation and failure flows of geomaterial using elastic-plastic soil constitutive model. *Int J Numer Anal Methods Geomech* 32(12):1537–1570
- Chen YF, Lin H, Wang YX, Xie SJ, Zhao YL, Yong WX (2021) Statistical damage constitutive model based on the Hoek–Brown criterion. *Archiv Civ Mech Eng* 21(3):117. <https://doi.org/10.1007/s43452-021-00270-y>
- Cheng SF, Ye Y, Zeng YW, Gao R, Qin XR (2023) Numerical investigation on the debonding of cement anchorage in clay rocks based on a hybrid FEM/DEM model. *Comput Geotech* 156:105276. <https://doi.org/10.1016/j.compgeo.2023.105276>
- Das R, Cleary PW (2010) Effect of rock shapes on brittle fracture using smoothed particle hydrodynamics. *Theor Appl Fract Mech* 53(1):47–60. <https://doi.org/10.1016/j.tafmec.2009.12.004>
- De Chant LJ (2005) Validation of a computational implementation of the Grady–Kipp dynamic fragmentation theory for thin metal plate impacts using an analytical strain-rate model and hydrodynamic analogues. *Mech Mater* 37(1):83–94. <https://doi.org/10.1016/j.mechmat.2003.12.008>
- Deng Y, Yin F, Deng HC, Li J, Liu W (2020) Research on crack propagation and rock fragmentation efficiency under spherical tooth dynamic indentation. *Arab J Geosci* 13(1):1–9. <https://doi.org/10.1007/s12517-019-4926-7>
- Dong XW, Liu GR, Li ZL, Zeng W (2016) A smoothed particle hydrodynamics (SPH) model for simulating surface erosion by impacts of foreign particles. *Tribol Int* 95:267–278. <https://doi.org/10.1016/j.triboint.2015.11.038>
- Douillet-Grellier T, Jones B, Pramanik R, Pan K, Albaiz A, Williams J (2016) Mixed-mode fracture modeling with smoothed particle hydrodynamics. *Comput Geotech* 79:73–85. <https://doi.org/10.1016/j.compgeo.2016.06.002>
- Drucker DC, Prager W (1952) Soil mechanics and plastic analysis or limit design. *Quart Appl Math* 10(2):157–165. <https://doi.org/10.1090/qam/48291>
- Drucker DC, Prager W, Greenberg HJ (1952) Extended limit design theorems for continuous media. *Quart Appl Math* 9(4):381–389. <https://doi.org/10.1090/qam/45573>
- Eftekhari M, Baghbanan A, Hashemolhosseini H (2016) Crack propagation in rock specimen under compressive loading using extended finite element method. *Arab J Geosci* 9(2):145. <https://doi.org/10.1007/s12517-015-2196-6>
- Fan H, Huang D, Wang G (2021a) A four-way enhanced numerical manifold method for crack propagation and failure analysis of rock slopes. *Appl Math Model* 95:623–643. <https://doi.org/10.1016/j.apm.2021.02.025>
- Fan H, Huang D, Wang G (2021b) Cone-complementary manifold method for stability and failure analysis of jointed/fractured rock masses. *Comput Geotech* 131:103955. <https://doi.org/10.1016/j.compgeo.2020.103955>
- Fu JW et al (2017) Simulating progressive failure in brittle jointed rock masses using a modified elastic-brittle model and the application. *Eng Fract Mech* 178:212–230. <https://doi.org/10.1016/j.engfracmech.2017.04.037>
- Giannakeas IN et al (2020) Coupling XFEM and peridynamics for brittle fracture simulation: part II—adaptive relocation strategy. *Comput Mech* 66(3):683–705. <https://doi.org/10.1007/s00466-020-01872-8>
- Grady DE, Kipp ME (1980) Continuum modelling of explosive fracture in oil shale. *Int J Rock Mech Min* 17(3):147–157. [https://doi.org/10.1016/0148-9062\(80\)91361-3](https://doi.org/10.1016/0148-9062(80)91361-3)
- Gray JP, Monaghan JJ (2004) Numerical modelling of stress fields and fracture around magma chambers. *J Volcanol Geotherm Res* 135(3):259–283. <https://doi.org/10.1016/j.jvolgeores.2004.03.005>
- Gray JP, Monaghan JJ, Swift RP (2001) SPH elastic dynamics. *Comput Meth Appl Mech Eng* 190(49–50):6641–6662. [https://doi.org/10.1016/S0045-7825\(01\)00254-7](https://doi.org/10.1016/S0045-7825(01)00254-7)
- Hu M, Gao T, Dong XW, Tan QT, Yi C, Wu F, Bao AH (2023) Simulation of soil-tool interaction using smoothed particle hydrodynamics (SPH). *Soil till Res* 229:105671. <https://doi.org/10.1016/j.still.2023.105671>
- Huang Y, Bao YJ, Zhang M, Liu C, Lu P (2015) Analysis of the mechanism of seabed liquefaction induced by waves and related seabed protection. *Nat Hazards* 79(2):1399–1408. <https://doi.org/10.1007/s11069-015-1897-1>
- Jiang MJ, Jiang T, Crosta GB, Shi ZM, Chen H, Zhang N (2015) Modeling failure of jointed rock slope with two main joint sets using a novel DEM bond contact model. *Eng Geol* 193:79–96. <https://doi.org/10.1016/j.enggeo.2015.04.013>
- Jiang H, Liu Z, Gao K (2017) Numerical simulation on rock fragmentation by discontinuous water-jet using coupled SPH/FEA method. *Powder Technol* 312:248–259. <https://doi.org/10.1016/j.powtec.2017.02.047>
- Kaus BJP (2010) Factors that control the angle of shear bands in geodynamic numerical models of brittle deformation. *Tectonophysics* 484(1–4):36–47. <https://doi.org/10.1016/j.tecto.2009.08.042>
- Keller A, Hutter K (2014) A viscoelastic damage model for polycrystalline ice, inspired by Weibull-distributed fiber bundle models. Part I: Constitutive models. *Continuum Mech Therm* 26(6):879–894. <https://doi.org/10.1007/s00161-014-0348-7>
- Lajtai EZ (1971) A theoretical and experimental evaluation of the Griffith theory of brittle fracture. *Tectonophysics* 11(2):129–156. [https://doi.org/10.1016/0040-1951\(71\)90060-6](https://doi.org/10.1016/0040-1951(71)90060-6)
- Li PF (2015) Study on model test of the process of the rocklike materials failure based on acoustic emission and image processing technology. Chongqing University, Chongqing
- Li Z, Ji C, Li Y, Xu LR (2007) The brittle fracture criterion based on the maximum tensile stress on the surface of blunt crack tip. *Mech Res Commun* 34(5–6):472–479. <https://doi.org/10.1016/j.mechrescom.2007.03.004>
- Liu XS et al (2016) Damage constitutive model based on energy dissipation for intact rock subjected to cyclic loading. *Int J Rock Mech Min* 85:27–32. <https://doi.org/10.1016/j.ijrmms.2016.03.003>
- Liu Y, Liu W, Wang C (2023) Mechanical properties and constitutive model of fractured red sandstone under acid corrosion. *SN Appl Sci* 5(7):1–13. <https://doi.org/10.1007/s42452-023-05415-7>
- Melosh H, Ryan E, Asphaug E (1992) Dynamic fragmentation in impacts—hydrocode simulation of laboratory impacts. *J Geophys*

- Res-Planet 97(E9):14735–14759. <https://doi.org/10.1029/92JE01632>
- Monaghan J (1992) Smoothed particle hydrodynamics. *Annu Rev Astron Astr* 30:543–574. <https://doi.org/10.1146/annurev.aa.30.090192.002551>
- Monaghan JJ (2000) SPH without a tensile instability. *J Comput Phys* 159(2):290–311. <https://doi.org/10.1006/jcph.2000.6439>
- Mu DR, Wen AH, Zhu DQ, Tang AP, Nie Z, Wang ZY (2022) An improved smoothed particle hydrodynamics method for simulating crack propagation and coalescence in brittle fracture of rock materials. *Theor Appl Fract Mec* 119:103355. <https://doi.org/10.1016/j.tafmec.2022.103355>
- Niu Y, Liu GJ, Zhong Z, Wang JG, Zhang RR, Liu BL (2023) Numerical investigation on fracture characteristic and failure mechanism of rock-like materials with intermittent flaws under compressive-shear loading. *Constr Build Mater* 388:131698. <https://doi.org/10.1016/j.conbuildmat.2023.131698>
- Rabczuk T, Ren H (2017) A peridynamics formulation for quasi-static fracture and contact in rock. *Eng Geol* 225:42–48. <https://doi.org/10.1016/j.enggeo.2017.05.001>
- Sharafisafa M, Nazem M (2014) Application of the distinct element method and the extended finite element method in modelling cracks and coalescence in brittle materials. *Comput Mater Sci* 91:102–121. <https://doi.org/10.1016/j.commatsci.2014.04.006>
- Singh A, Seshagiri Rao K, Ayothiraman R (2019) A closed-form analytical solution for circular opening in rocks using Drucker–Prager criterion. *Indian Geotech J* 49(4):437–454. <https://doi.org/10.1007/s40098-019-00358-6>
- Sun X, Sakai M, Yamada Y (2013) Three-dimensional simulation of a solid–liquid flow by the DEM–SPH method. *J Comput Phys* 248:147–176. <https://doi.org/10.1016/j.jcp.2013.04.019>
- Wang CL, He BB, Hou XL, Li JY, Liu L (2020) Stress-energy mechanism for rock failure evolution based on damage mechanics in hard rock. *Rock Mech Rock Eng* 53(3):1021–1037. <https://doi.org/10.1007/s00603-019-01953-y>
- Wang ZL (2018) Study on mechanical properties and failure law of single fractured rock-like material under uniaxial compression. Yangtze University. Available at: https://kns.cnki.net/kcms2/article/abstract?v=3uoqIhG8C475K0m_zrgu4lQARvvp2SAkZIGkvqfmUZglMdu7fCR484ebBRzodA8D5lUJsv0NvHwQ2dSL1V321_Sj_Kihyrfu&uniplatform=NZKPT
- Yang JP, Chen WZ, Yang DS, Yuan JQ (2015) Numerical determination of strength and deformability of fractured rock mass by FEM modeling. *Comput Geotech* 64:20–31. <https://doi.org/10.1016/j.compgeo.2014.10.011>
- Yang SQ, Tian WL, Ranjith PG, Liu XR, Chen M, Cai W (2022) Three-dimensional failure behavior and cracking mechanism of rectangular solid sandstone containing a single fissure under triaxial compression. *Rock Mech Bull* 1(1):100008. <https://doi.org/10.1016/j.rockmb.2022.100008>
- Zhai SF, Zhou XP, Bi J, Xiao N (2016) The effects of joints on rock fragmentation by TBM cutters using general particle dynamics. *Tunn Undergr Sp Tech* 57:162–172. <https://doi.org/10.1016/j.tust.2016.01.035>
- Zhang T, Zhou XP (2023) Ordinary state-based peridynamic plastic model with Drucker–Prager criterion considering geometric nonlinearity. *Appl Math Model* 118:212–235. <https://doi.org/10.1016/j.apm.2023.01.007>
- Zheng L, Wu YH, Wu W, Zhang H, Peng XY, Zhang XL, Wu XZ (2021) Efficient investigation of rock crack propagation and fracture behaviors during impact fragmentation in rockfalls using parallel DDA. *Adv Civ Eng*. <https://doi.org/10.1155/2021/5901561>
- Zhou X, Chen J (2019) Extended finite element simulation of step-path brittle failure in rock slopes with non-persistent en-echelon joints. *Eng Geol* 250:65–88. <https://doi.org/10.1016/j.enggeo.2019.01.012>
- Zhou C et al (2020) A new damage model accounting the effect of joint orientation for the jointed rock mass. *Arab J Geosci* 13(7):295. <https://doi.org/10.1007/s12517-020-5274-3>

Publisher's Note Springer Nature remains neutral with regard to jurisdictional claims in published maps and institutional affiliations.

Springer Nature or its licensor (e.g. a society or other partner) holds exclusive rights to this article under a publishing agreement with the author(s) or other rightsholder(s); author self-archiving of the accepted manuscript version of this article is solely governed by the terms of such publishing agreement and applicable law.